

Mid-infrared optical properties of thin films of aluminum oxide, titanium dioxide, silicon dioxide, aluminum nitride, and silicon nitride

Jan Kischkat,^{1,*} Sven Peters,² Bernd Gruska,² Mykhaylo Semtsiv,¹
Mikaela Chashnikova,¹ Matthias Klinkmüller,¹ Oliana Fedosenko,¹
Stephan Machulik,¹ Anna Aleksandrova,¹ Gregorii Monastyrskiy,¹
Yuri Flores,¹ and W. Ted Masselink¹

¹Humboldt-Universität zu Berlin, Newtonstrasse 15, 12489 Berlin, Germany

²Sentech Instruments GmbH, Schwarzschildstrasse 2, 12489 Berlin, Germany

*Corresponding author: kischkat@physik.hu-berlin.de

Received 4 June 2012; revised 27 August 2012; accepted 28 August 2012;
posted 28 August 2012 (Doc. ID 169946); published 26 September 2012

The complex refractive index components, n and k , have been studied for thin films of several common dielectric materials with a low to medium refractive index as functions of wavelength and stoichiometry for mid-infrared (MIR) wavelengths within the range 1.54–14.29 μm (700–6500 cm^{-1}). The materials silicon oxide, silicon nitride, aluminum oxide, aluminum nitride, and titanium oxide are prepared using room temperature reactive sputter deposition and are characterized using MIR variable angle spectroscopic ellipsometry. The investigation shows how sensitive the refractive index functions are to the O_2 and N_2 flow rates, and for which growth conditions the materials deposit homogeneously. It also allows conclusions to be drawn on the degree of amorphousness and roughness. To facilitate comparison of the materials deposited in this work with others, the index of refraction was also determined and provided for the near-IR and visible ranges of the spectrum. The results presented here should serve as a useful information base for designing optical coatings for the MIR part of the electromagnetic spectrum. The results are parameterized to allow them to be easily used for coating design. © 2012 Optical Society of America

OCIS codes: 310.6860, 310.1210.

1. Introduction

Optical applications in the mid-infrared (MIR) part of the spectrum generally require components to include optical coatings appropriate for the MIR to modify their wavelength-dependent reflectivity and transmissivity characteristics. One example is MIR light sources, such as the quantum-cascade laser (QCL) that is finding increasing use in gas spectroscopy and gas imaging [1], especially within the wavelength range of 3–12 μm . Applications include

medical breath analysis for early prediagnosis, environmental gas analysis, and remote sensing. Proper laser design requires facet coatings to optimize their reflectivity for that particular laser. Many coatings are designed to be either highly reflective (HR) or antireflective (AR) and, although the HR coatings need not be transparent, the AR coatings need to both reduce the reflectivity and remain transparent within the target wavelength range. Certain applications of AR coatings require residual reflectivity to be as low as 10^{-3} – 10^{-4} over a range of hundreds of reciprocal centimeters.

Design and fabrication of these coatings requires accurate knowledge of the complex refractive index

components, n and k , in the region of interest for the materials in use. Furthermore, accurate information is necessary on how to adjust the refractive index to reach a desired value in order to reduce the number of layers needed for a given application. Finally, to allow for more flexibility when designing multilayer coatings, a certain spectrum of attainable refractive indices needs to be covered. But finding low refractive index materials to complement high index materials such as silicon or germanium in IR multilayer coatings is not an easy task [2–4]. Most materials are not transparent enough, and the limits of the transparent regions are not clearly defined in most sources. One soon resorts to more exotic materials “to be safe.” These tend to have other significant drawbacks, most notably radioactivity in the case of thorium fluoride, hygroscopicity for sodium chloride, or simply significant internal stresses that make the materials not depositable at the thicknesses required for long wavelengths. Another obstacle is the added cost of installing the necessary health and safety precautions needed to evaporate toxic compounds, e.g., zinc selenide and zinc sulfide. This paper addresses the matter from a different angle. It revisits some common and nonhazardous materials that are known to deposit well under most conditions and accurately tabulates the refractive index and extinction coefficient for films of typical thicknesses in a wide spectral range, including at and around the absorption bands. This is to provide coating designers with the necessary information to determine where the absorption has tailed off to an acceptable level for their specific application.

Reactive sputtering is a useful tool to create thin films of sufficient quality to serve as optical coatings and has been a routine method for the various regions of the optical spectrum for many years [5]. Typically, the important parameters to control are the plasma power of the inert gas plasma (usually argon), the flow rates of both the inert gas and the reactive gas(es) (usually oxygen and/or nitrogen), and the residual pressure within the vacuum chamber.

Simple models predicting the stoichiometry of reactively sputtered alloys are available [6], but some stoichiometries require very precise control of the process parameters. In the simple case for which overstoichiometric deposition can be neglected, the relative concentration will vary between two extreme values depending on reactive gas flow; an example of this situation is the Ti–TiN system. In this case, the dielectric function is insensitive to the microscopic structure of the compound and the intermediate compositions can be accurately interpolated between the limiting values using effective intermediate theories [7]. Greater difficulties arise when the microscopic structure is relevant for the dielectric properties, as for the case of the TiO_x system. Here, not only do the different oxidization levels of titanium need to be considered, but even the limiting case of TiO_2 has multiple anisotropic microcrystallite phases, rutile

and anatase, with very different bulk indices of refraction, and an amorphous phase with varying degrees of density.

The current study determines which of the investigated materials are simple with respect to their behavior in the MIR and which need further investigation when in question for use as optical coatings. For this we present the refractive index functions for SiO_x , SiN_x , AlO_x , AlN_x , and TiO_x measured between 1.54 and 14.29 μm deposited at ambient temperatures, with different stoichiometries determined by the flow rate of the reactive gas.

The optical characterizations have been performed using MIR spectroscopic ellipsometry [7]. The single layers of the investigated materials deposited on a substrate (Si) were treated as multilayer structures to investigate possible optical gradients within the layers.

2. Experiment

We have fabricated for each of the five material systems—silicon oxide, silicon nitride, aluminum oxide, aluminum nitride, and titanium oxide—a series of single-layer coating samples with varying oxide and nitride content, each on single-side polished silicon substrates, with a total of 20 distinct deposition conditions. Including numerous tests for reproducibility, there were 38 samples in all. As targets we have used silicon, aluminum, titanium, and titanium dioxide. The samples had an area of approximately 1 cm^2 . They were subsequently analyzed with the use of IR variable angle spectroscopic ellipsometry.

A. Sputter Deposition

The rf sputter deposition system consists of a water-cooled target and sample table in a vacuum chamber, a rotary vane pump with a turbomolecular pump (Oerlikon Leybold Vacuum Turbovac TW 290 H), gas inlets with mass flow controllers (MKS Instruments SP10K), an rf generator for the plasma (VEB, TuR KW 4-1), and various measurement devices to control the vacuum, plasma, and gas flow. The vacuum chamber is a modified VEB Hochvakuum Dresden R HVG 32, a glass bell-jar type. The target and sputter table serve as electrodes for the rf electric field. The thickness of the deposited film was measured *in situ* with a quartz oscillator that was placed next to the sample and coated along with it; it was later determined precisely with ellipsometry.

The residual pressure in the chamber prior to the inlet of the sputter gases was $2 \cdot 10^{-4}$ Pa. During sputtering, the 36 SCCM (SCCM denotes cubic centimeters per minute at standard temperature and pressure) of argon influx resulted in an equilibrium chamber pressure of 0.6 Pa. The resulting partial pressures for the gases at different flow rates are given in Table 1. Due to the spatial variation in pressure in the chamber due to the highly nonequilibrium setup, there is a low degree of confidence in these values. The plasma had powers of 200–600 W depending on the sample at an electric-field frequency of

Table 1. Resultant Partial Pressures of O₂ and N₂ in Sputter Chamber for Given Influx While Vacuum Pumps Are Running

Gas Flow in SCCM	Partial Pressure in Pa
4	$6 \cdot 10^{-2}$
2	$3 \cdot 10^{-2}$
1.8	$2.6 \cdot 10^{-2}$
1.6	$2.3 \cdot 10^{-2}$
1.4	$2.0 \cdot 10^{-2}$

27.12 MHz and a dc acceleration voltage of 7–16 V depending on the sample. The standing-wave ratio of the coupling network was 1.1 on all samples.

The sputter targets were 3 in. diameter Si (undoped, 99.999% pure), Al (99.999% pure), Ti (99.995% pure), and TiO₂ (99.9% pure), from KJ Lesker. To clean the targets, they were oxidized in oxygen plasma for 60 s after insertion and the top layer was sputtered off during 20 min runs of nonreactive, pure-argon sputtering without a sample in the chamber. The target and substrate temperatures were not directly controlled.

B. Spectroscopic Ellipsometry

Ellipsometry measures the change of the polarization state of light reflected from the surface of a sample at non-normal incidence. The polarization state changes, because components of the electric field vector parallel and perpendicular to the plane of incidence on a surface have different complex Fresnel amplitude reflection coefficients. These, in turn, are related to the optical properties and optical thicknesses of the samples under investigation. Ample literature is available on the theory of ellipsometry (see, e.g., [7]).

Spectroscopic ellipsometry measurements were performed using two different ellipsometers, both manufactured by Sentech Instruments. The MIR model SENDIRA was used in the range of 700–6500 cm⁻¹, and the visible to near-infrared (VIS-NIR) range of 4000–30,000 cm⁻¹ was covered by the model SE-850. Both employ a retarder plate to allow for data acquisition in the entire range of 0–2 π for the ellipsometric parameter Δ (for definition of the ellipsometric parameters Ψ and Δ , see [7]). The SENDIRA employs a Fourier transform IR spectrometer (FTIR) model 640 MIR by Agilent as a radiation source with either a mercury cadmium telluride (MCT) or doped triglycine sulfate (DTGS) detector. The SE-850 uses a Xe arc lamp (NIR-VIS-UV) as a light source and a polychromator with a diode array (NIR-VIS-UV) and an FTIR spectrometer (NIR) as detectors. They both use an autocollimating telescope and microscope for sample alignment. The software SpectraRay/3 was used to fit the ellipsometric Ψ and Δ curves and calculate the optical properties according to the physical models described in Section 3.

3. Dispersion models

Spectroscopic ellipsometry provides optical properties by fitting open (semi-)empirical parameters in

model dispersion relations for the layers to the overall Ψ and Δ functions measured for the samples to yield the correct dispersion relations for each material [7].

Different mathematical models are used to approximate n and k , the simplest being a constant, e.g., 1 for air. Others either model n and k empirically like the Cauchy model or model the complex dielectric function $\epsilon = \epsilon_1 + i\epsilon_2 = \tilde{n}^2 = (n + ik)^2$, where \tilde{n} is the complex index of refraction, in a more or less sophisticated manner from first principles.

Others, like the Tauc–Lorentz Model [8], take the joint density of states of the materials into consideration and calculate the imaginary part of the dielectric function, from which the entire dielectric function is then derived by Kramers–Kronig integration [9].

A short introduction to the Brendel oscillator model, which is the model of choice for the MIR in this work, is given in the next section.

A. The Brendel Oscillator Model

The Brendel oscillator model is a versatile tool used to model absorption bands in (partially) amorphous solids and is the model used for the MIR range in this study.

The model is based on the Drude–Lorentz (DL) model that treats each discrete vibrational mode as a classical damped harmonic oscillator, which accounts for the main features of an absorption line—center frequency, line width, and oscillator strength—in a straightforward way. The DL model uses a dielectric function of the form

$$\epsilon_{\text{DL}}(\nu) = \epsilon_{\infty} + \sum_{j=1}^m X_j(\nu), \quad (1)$$

where

$$X_j(\nu) = \frac{\nu_{pj}^2}{\nu_{0j}^2 - \nu^2 - i\nu_{\tau j}\nu} \quad (2)$$

is the contribution of each vibrational mode j . Here, for each mode j , ν_{0j} is the center frequency, ν_{pj} is the plasma frequency, i.e., the strength of the oscillator, and $\nu_{\tau j}$ is the damping constant. The high-frequency permittivity ϵ_{∞} is due to the electronic polarizability. A dielectric function of this form obeys the Kramers–Kronig relation.

The Brendel oscillator model is similar to the DL model, but instead of m discrete oscillators as in the DL model, the Brendel model includes m distributions of oscillators. Thus, each Brendel oscillator is an inhomogeneously broadened DL oscillator, i.e., the number of DL oscillators per frequency interval around a center frequency are governed by a Gaussian distribution. The inhomogeneous broadening allows for a further degree of freedom associated with a partial amorphousness of the absorbing material and therefore yields a better fit with fewer parameters. A dielectric function with Brendel oscillators,

each of which is a convolution of a Gaussian function with Lorentz oscillators, by design fulfills the Kramers–Kronig relation as well. The dielectric function also has the form of Eq. (1), where the oscillators now have the form

$$X_j(\nu) = \frac{1}{\sqrt{2\pi}\sigma_j} \int_{-\infty}^{\infty} \exp\left(-\frac{(x - \nu_{0j})^2}{2\sigma_j^2}\right) \frac{\nu_{pj}^2}{x^2 - \nu^2 - i\nu_{vj}\nu} dx, \quad (3)$$

where σ_j is the standard deviation of the Gaussian distribution. The ratio ν_{vj}/σ_j determines the shape of the imaginary part from purely Drude-like to purely Gaussian.

In using the Brendel model, there are two different schools of thought regarding assigning Brendel oscillators to absorption features in the measured Ψ and Δ curves. One is to use as few oscillators as can be supported by physical arguments, i.e., with real vibrational transitions, whether or not the Ψ and Δ curves can actually be well approximated by these only. Another approach is to use as many oscillators as needed to fit the spectra well, even though this may require the use of oscillators without a physical basis. In defense of this approach, it can be argued that the n and k functions of the material, be it pure or contaminated by traces of other substances, will be more accurate. Further, the use of “unphysical” oscillators can be justified in case there are sharp features in the joint density of states within the range of broad absorption lines. Since these features migrate to the absorption spectrum, they give the impression that additional sharp transitions are present and can therefore be emulated by adding further oscillators. Since this work is only interested in giving the most accurate n and k values possible, the latter approach is chosen.

B. Effective Intermediate Layers

Analytical models that describe the interference in a stack of layers evaluated by the ellipsometer’s software presume homogeneous layers with perfectly sharp, parallel interfaces. Although this ideal case can be realized in some cases, a feasible way has to be found to treat the more general case, including the likes of inhomogeneities or interface roughnesses within the same framework. A very powerful method is to introduce effective intermediate layers between two other materials with the optical constant being some interpolation between the adjacent materials. A description of physically sensible interpolation mechanisms can be found in [7]. In the case of an interface roughness, this is a good approximation if the average grain size of the roughness is much smaller than the wavelength of the light.

If the deposition environment parameters drift over time and introduce a gradient between two sets of values, this gradient can be approximated by a finite number of effective intermediate layers. The interpolation between the values of the refractive

index of the extremes then changes from layer to layer according to some translation rule.

4. Results

In this section we present the measured optical properties in the form of graphs and tables of the fit parameters that were used to fit the dispersion models to the measured data. For best readability, the graphs displayed in this section all have different scales to highlight features of the individual series. The refractive index components n (plotted black) and k (plotted gray) are mostly drawn into the same graph with the same line style corresponding to the same flow rate. Where k is omitted, the material is transparent to within the limits of the measurement.

The transparency criterion is based on whether more than 99% of the intensity passes through a quarter-wave plate of the material. It therefore takes both components of the refractive index n and k into consideration. The significance of a thickness equivalent to a quarter wave is evident when considering single-layer antireflection coatings. This criterion, although arbitrary, is applied for practical purposes.

The value of the mean square error (MSE) as an unbiased maximum likelihood estimator used as the merit function of the fit by the manufacturer is listed for reference purposes. It is the square of σ as used, for instance, by Fujiwara in [10] (p. 199). For a quantitative analysis of how the MSE relates to the accuracy of n and k for each wavelength, strictly speaking, the full covariance matrix of all fit parameters needs to be considered [11]. For the given purposes, though, it should suffice to state that if the fit is good enough for the MSE to exhibit values in the range of 1–3, the relative errors of n and k at any given point will not exceed 10^{-2} – 10^{-3} .

The values of the fitted parameters displayed in Tables 2–6 are to be used in order to reproduce spectra and not primarily as an indication of the underlying physical absorption mechanisms. The ellipsometric curves were fitted with as many parameters as were necessary for the desired accuracy and correlations were not fully avoided. Thus, the parameters are not unique, but the same optical properties can be calculated for different sets of solutions from the manifold of solutions.

The sample names (e.g., SO14-200) used in the following sections reflect the material (SO for silicon oxide), reactive gas flow rate (14 for 1.4 SCCM), and sputter power (200 W).

A. Silicon Dioxide

Silicon dioxide is the classic material mentioned in conjunction with the sputter deposition technology, and ample information is available [12]. In this work, we list the properties in order to have a stable reference point to compare with other materials. The samples SO14-200, SO16-200, SO18-200, SO20-200, and SO40-200 had layer thicknesses 525, 486, 558, 510, and 1503 nm, respectively. Table 2 shows the Brendel oscillator parameters used to fit the spectra given in

Table 2. Brendel Oscillator Parameters for Silicon Dioxide with the Resulting MSE (ν_{0j} , ν_{tj} , ν_{pj} , σ_j are in cm^{-1})

Sample	$\epsilon_1(\infty)$	ν_{01}	ν_{t1}	ν_{p1}	σ_1	ν_{02}	ν_{t2}	ν_{p2}	σ_2	ν_{03}	ν_{t3}	ν_{p3}	σ_3	ν_{04}	ν_{t4}	ν_{p4}	σ_4	ν_{05}	ν_{t5}	ν_{p5}	σ_5	MSE
SO14-200	2.09	1046	1.55	575	76	1167	0.51	288	125	1058	10.57	459	63	798	55.30	415	170					1.036
SO16-200	2.09	1046	0.59	579	78	1167	1.23	290	125	1058	8.52	457	62	798	54.95	406	180					1.261
SO18-200	2.08	1046	7.20	589	77	1167	1.20	287	123	1058	2.24	436	67	798	54.16	401	147					1.200
SO20-200	2.10	1046	3.37	572	81	1167	0.91	299	127	1058	0.93	456	64	225	53.76	443	297	799	9.10	234	128	1.448
SO40-200	2.09	1046	15.53	544	63	1167	4.43	309	122	1058	0.42	466	67	434	54.14	427	316	799	12.94	223	85	1.382

Table 3. Brendel Oscillator Parameters for Silicon Nitride with the Resulting MSE (ν_{0j} , ν_{tj} , ν_{pj} , σ_j are in cm^{-1})

Sample	$\epsilon_1(\infty)$	ν_{01}	ν_{t1}	ν_{p1}	σ_1	ν_{02}	ν_{t2}	ν_{p2}	σ_2	ν_{03}	ν_{t3}	ν_{p3}	σ_3	ν_{04}	ν_{t4}	ν_{p4}	σ_4	ν_{05}	ν_{t5}	ν_{p5}	σ_5	MSE
SN14-300	5.68	697	57	54	12	810	2	792	157	941	3	556	152	1062	211	40	207	1208	1917	772	1045	0.797
SN16-300	3.90	826	6	920	205	925	10	522	208	1060	6	450	825	1189	3253	2428	32,235	17,873	0	22,377	0	0.692
SN18-300	3.06	826	20	1247	294	925	201	433	440	1063	2	100	781	1185	0	191	355	22128	0	37,337	0	0.923
SN20-300	6.12	826	2	1240	283	925	4	1	44	1063	36	63	3468	1185	57	702	592	7931	1	0	2987	0.916
SN40-300	3.55	826	12	902	171	925	0	664	163	1063	58	379	145	1185	44	172	104	2577	0	235	588	1.975

Table 4. Brendel Oscillator Parameters for Titanium Dioxide with the Resulting MSE (ν_{0j} , ν_{tj} , ν_{pj} , σ_j are given in cm^{-1})

Sample	$\epsilon_1(\infty)$	ν_{01}	ν_{t1}	ν_{p1}	σ_1	ν_{02}	ν_{t2}	ν_{p2}	σ_2	MSE
TO16-200	6.15	23	78	2020	410	10,983	2	180	65	0.705
TO20-200	5.83	46	18	1878	732	10,815	160	4590	387	0.765
TD00-600	5.47	90	16	1827	829	14,030	1	8985	146	0.773

Table 5. Brendel Oscillator Parameters for Aluminum Oxide with the Resulting MSE (ν_{0j} , ν_{tj} , ν_{pj} , σ_j are in cm^{-1})

Sample	$\epsilon_1(\infty)$	ν_{01}	ν_{t1}	ν_{p1}	σ_1	ν_{02}	ν_{t2}	ν_{p2}	σ_2	ν_{03}	ν_{t3}	ν_{p3}	σ_3	MSE
AO18-200	2.08	601	2.26	824	957	744	5.7	524	202	224,363	0	43,887	0	1.388
AO20-200	2.11	190	18	735	1286	715	0	726	254	221,086	0	43,193	0	1.331
AO40-200	2.12	79	1	921	843	784	47	581	179	217,457	1	43,199	0	1.212

Figs. 1–3. We used 4–5 oscillators, decided by numerical rationale. As can be seen, silicon dioxide deposits stoichiometrically within a wide range of the sputter parameters, using a silicon target and O_2 as a reactant gas. Testing the lower end of the O_2 flux down to 1.4 SCCM, we have not been able to deposit substoichiometric $\text{Si}_{1+x}\text{O}_{2-x}$. Accordingly, the refractive index is largely independent of the O_2 flux. The deposition rate is also stable for the different O_2 fluxes, which at a plasma power of 200 W and Ar flux of 36 SCCM is $(7 \pm 0.2) \text{ nm/min}$. In the VIS there is no measurable extinction coefficient, and the index of refraction is virtually identical within an error of 0.005; at the He–Ne wavenumber of 15803 cm^{-1} , $n_{\text{SO40-200}} = 1.459$ and $n_{\text{literature}} = 1.457$ [13,14]. The

material deposits homogeneously over time with no appreciable surface roughness.

Figure 1 shows the refractive index in the further MIR from 700 to 2000 cm^{-1} . SiO_2 has a small absorption peak between 700 and 900 cm^{-1} (gray curve) and its strong Reststrahlen peak between 950 and 1300 cm^{-1} . Due to the strength of these peaks, the index of refraction undershoots the value of vacuum between approximately 1100 and 1350 cm^{-1} . It then increases steadily to 1.43 at 4500 cm^{-1} (Fig. 2) and slowly to 1.48 at $30,000 \text{ cm}^{-1}$ (Fig. 3). SiO_2 is transparent for wavenumbers $\nu > 1560 \text{ cm}^{-1}$. There is very little inhomogeneous broadening, although SiO_2 deposits amorphously, which is mainly due to the high short-distance ordering present in SiO_2 .

Table 6. Brendel Oscillator Parameters for Aluminum Nitride with the Resulting MSE (ν_{0j} , ν_{tj} , ν_{pj} , σ_j are given in cm^{-1})

Sample	$\epsilon_1(\infty)$	ν_{01}	ν_{r1}	ν_{p1}	σ_1	ν_{02}	ν_{r2}	ν_{p2}	σ_2	ν_{03}	ν_{r3}	ν_{p3}	σ_3	ν_{04}	ν_{r4}	ν_{p4}	σ_4	ν_{05}	ν_{r5}	ν_{p5}	σ_5	MSE
AN18-300	5.72	588	0	2847	22.3	1207	0	1025	365	769	0	123	13.4	2648	392	4260	1009	10,690	10,587	25,970	487	1.299
Sample	$\epsilon_1(\infty)$			ν_{01}	ν_{r1}			ν_{p1}	σ_1		ν_{02}	ν_{r2}		ν_{p2}	σ_2		ν_{03}	ν_{r3}		ν_{p3}	σ_3	MSE
AN20-300	4.15			797	39			467	178		662	10		989	189		215	54		323	229	3.142
AN20-200	2.95			824	38			400	290		592	10		1093	120		257	54		312	203	3.142
AN40-200	2.89			620	0			1030	428													2.072

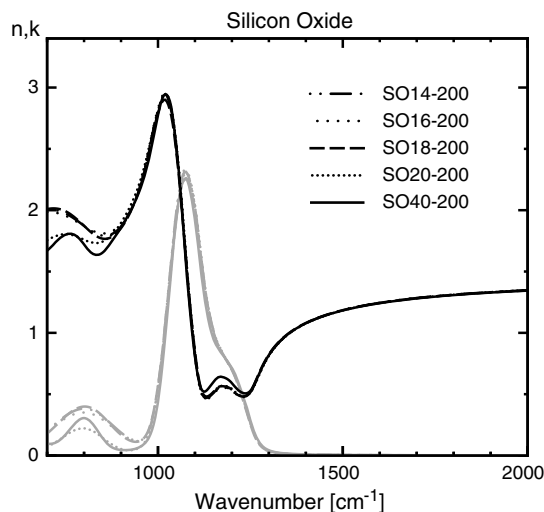


Fig. 1. Real (black curves) and imaginary (gray curves) parts of the refractive index for SiO_2 in the further IR part of the MIR spectrum at different reactive gas flow rates.

The spectra, in fact, show very close agreement to spectra that are modeled with a single Lorentz oscillator at the transverse-optical (TO) phonon frequency, as would be the case for a simple model of the diatomic, periodic lattice in the harmonic approximation.

Figure 2 shows the nearer MIR region between 2000 and 6500 cm^{-1} , which is transparent, and the refractive index rises from approximately 1.345 at 2000 cm^{-1} to approximately 1.44 at 6500 cm^{-1} . Figure 3 illustrates the NIR and VIS range up to 30,000 cm^{-1} with normal dispersion; the refractive index grows to approximately 1.48. The latter was modeled with a simple Cauchy relationship.

B. Silicon Nitride

Table 3 shows the Brendel oscillator parameters used to fit the spectra given in Figs. 4–6. We used five oscillators to fit each spectrum. The samples SN14-300, SN16-300, SN18-300, SN20-300, and SN40-300 had layer thicknesses of 465, 413, 554, 437, and 726 nm, respectively. A noticeable difference between the SiN_x as seen in Fig. 4 and the SiO_2 as seen in Fig. 1 is the strong inhomogeneous broadening of the absorption peaks centered at $\approx 900 \text{ cm}^{-1}$.

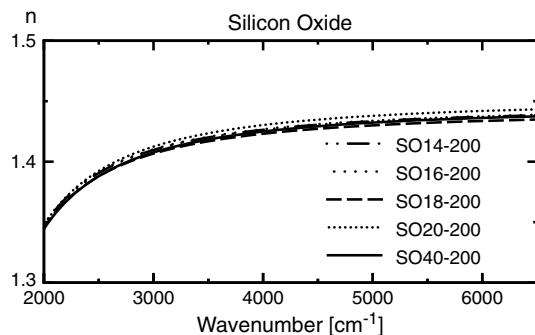


Fig. 2. Real refractive index for SiO_2 in the nearer IR part of the MIR spectrum at different reactive gas flow rates.

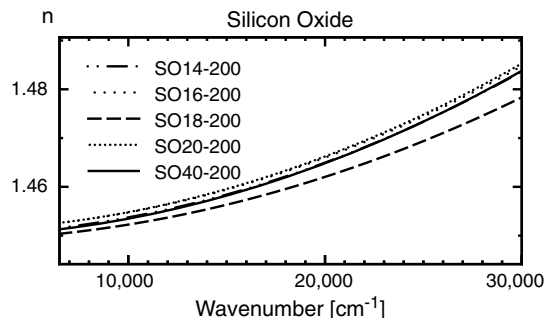


Fig. 3. Real refractive index for SiO_2 in the visible spectrum at different reactive gas flow rates.

This feature implies a high degree of amorphousness of the sputtered SiN_x .

An additional difference between sputtered SiN_x and SiO_2 is that the properties of the SiN_x sputtered using a Si target depend on the N_2 flux within the range of fluxes tested. Figures 4 and 6 show a transition region between the semiconductor and the dielectric in the sense that below 4 SCCM of N_2 flux, the refractive index shows characteristics of both semiconducting silicon and insulating stoichiometric Si_3N_4 that vary as the flow is varied. The absorption peak in Fig. 4 that has an onset below the lower measured spectral limit and extends to approximately 1200 cm^{-1} is due to the vibrations of the diatomic basis of silicon nitride and is not a feature of pure silicon. This absorption peak grows in amplitude as the nitrogen content is raised. Also, as is apparent from Fig. 6, using a Tauc–Lorentz model for the visible range, the materials with flux rates below 4 SCCM exhibit a bandgap. The data, for example, from sample SN14-300 sputtered at 1.4 SCCM N_2 can be fitted to $E_g = 1.26 \text{ eV}$; pure silicon has $E_g \approx 1.1 \text{ eV}$, with higher values occurring for amorphous silicon. For higher nitrogen content, the bandgap is fitted to higher energies and the absorption

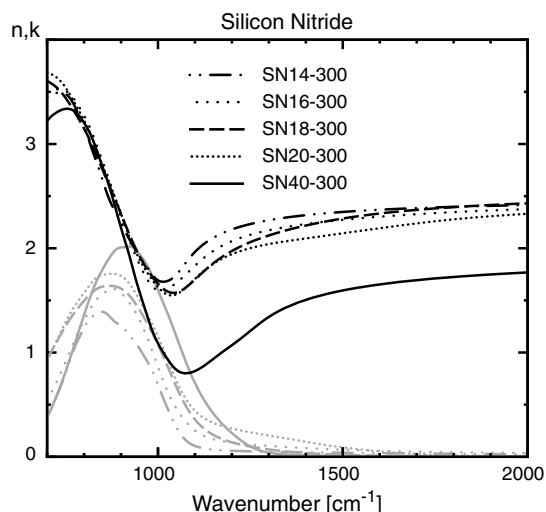


Fig. 4. Real (black curves) and imaginary (gray curves) parts of the refractive index for SiN_x in the further IR part of the MIR spectrum at different reactive gas flow rates.

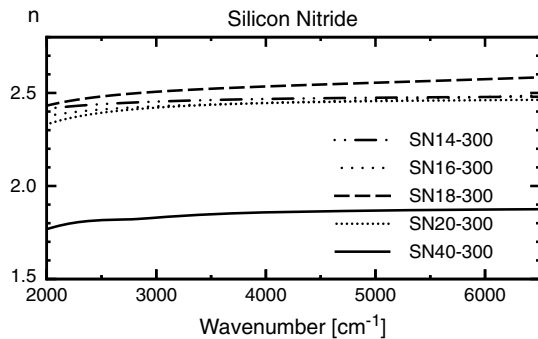


Fig. 5. Real refractive index for SiN_x in the nearer IR part of the MIR spectrum at different reactive gas flow rates.

weakens, until for 4 SCCM (SN40-300) the absorption is near the limit of detectability.

Nearly stoichiometric Si_3N_4 at 300 W was deposited with a N_2 flux of 4 SCCM (sample SN40-300) with an Ar flux of 36 SCCM. At the He-Ne wavenumber of 15803 cm^{-1} , the index of refraction $n_{\text{SN40-300}} = 1.904$, compared to the literature value of $n_{\text{literature}} = 2.011$; therefore, the material is still slightly substoichiometric [15]. The sputter rate is approximately $(10 \pm 0.7)\text{ nm/min}$ with no apparent dependence on the nitrogen flux. Due to the strong dependence on the nitrogen environment, it is crucial to allow the system enough time to reach a stable equilibrium before starting the sputtering process. Also, the target needs to be prepared in order to have a sufficiently pure surface. In the samples presented in this work, there was a slight composition gradient on the first few tens of nanometers.

The refractive index functions for N_2 flow rates in the range of 1.4–2 SCCM (samples SN14-300 through SN20-300) are noticeably different than for 4 SCCM (SN40-300) and depend fairly monotonically on the flow rate as seen in Fig. 5. For NIR and VIS wavelengths, the index of refraction for stoichiometric Si_3N_4 varies only gradually between ≈ 1.77

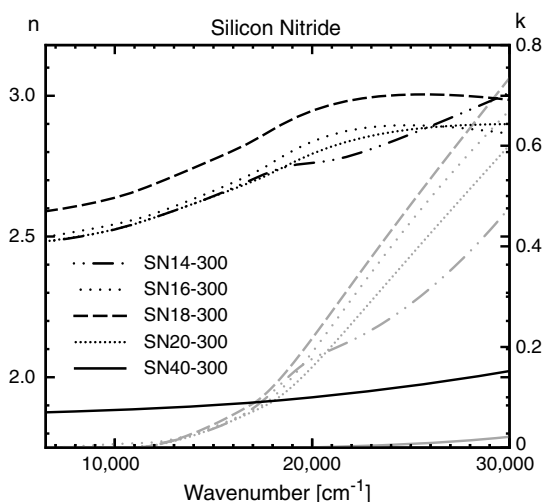


Fig. 6. Real (black curves) and imaginary (gray curves) parts of the refractive index for SiN_x in the visible spectrum at different reactive gas flow rates. Note the different scales for n and k .

and ≈ 1.87 and reaches a value of 2 in the UV, as can be seen in Fig. 6. This material is also transparent starting at 2900 cm^{-1} .

C. Titanium Dioxide

Table 4 shows the Brendel oscillator parameters used to fit the refractive index spectra for TiO_2 given in Figs. 7–9. Two oscillators were sufficient to fit each spectrum with very good accuracy. The TiO_2 was sputtered under three different conditions: samples TO16-200 and TO20-200 used a Ti sputter target with 1.6 and 2.0 SCCM O_2 flow, respectively, and sample TD00-600 used a TiO_2 target with no additional O_2 . The samples TO16-200, TO20-200, and TD00-600 had layer thicknesses 499, 553, and 352 nm, respectively.

Similar to earlier investigations (e.g., [16,17]), we observe that the layers are inhomogeneous in composition along the layer normal. After a ramp-up of about 140 nm, however, the conditions stabilize and the deposition becomes homogeneous. Although titanium allows for a multitude of different degrees of oxidation, we do not attribute the starting phase to a gradient in the relative concentration of titanium and oxygen but to a structural gradient, such as physical density or partial ordering by the following argument: when comparing the optical properties of the three layers at similar distances from the substrate, it can be found that they are very similar for all three samples. However, we imagine sample TD00-600 to be stoichiometric titanium dioxide even during the ramp-up because of the high binding energy of titanium and oxygen that makes their selective sputtering and pumping highly improbable [16] at the given plasma power. Rather, the temperature-dependent tendency of TiO_2 to granulate into microcrystallites of its different phases, rutile and anatase, whose structure, orientation, and distribution within the predominant amorphous phase contribute to the

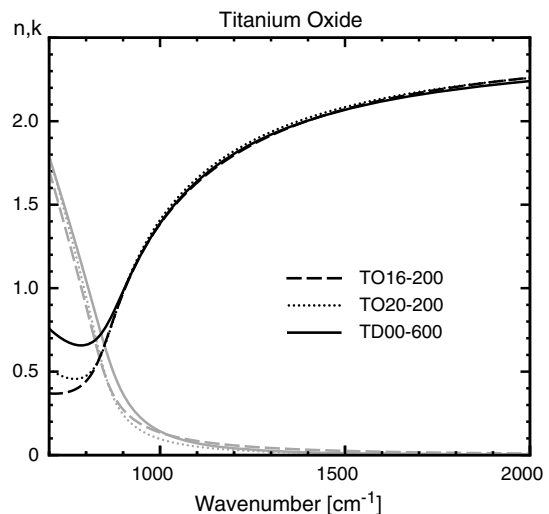


Fig. 7. Real (black curves) and imaginary (gray curves) parts of the refractive index for TiO_2 in the further IR part of the MIR spectrum at different reactive gas flow rates and targets.

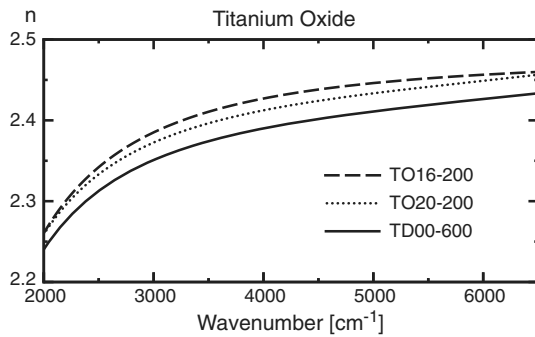


Fig. 8. Real refractive index for TiO_2 in the nearer IR part of the MIR spectrum at different reactive gas flow rates and targets.

optical properties, should be responsible for the initial gradient. A less dense deposition at lower temperatures is also likely [17].

Given in Figs. 7–9 are the complex refractive index functions of the homogeneous layers after the ramp-up. There were no experimentally significant differences between samples TO16-200 and TO20-200, and their refractive index was only slightly higher than that of sample TD00-600 (Fig. 8). Much larger differences in values within the VIS-NIR are typically found in the existing literature [13,17,18]. The sputter rate is approximately 0.9 nm/min at a power of 200 W for samples TO16-200 and TO20-200 and 4 nm/min at a power of 600 W for sample TD00-600. The materials were transparent for $\nu > 1680 \text{ cm}^{-1}$. Since TiO_2 is a large-bandgap semiconductor, use of the Tauc–Lorentz dispersion model is justified in the VIS, yielding fitted bandgaps of 3.12 eV for TO16-200 and TO20-200 and 3.15 eV for TD00-600. The index of refraction at the He–Ne wave number of 15803 cm^{-1} for sample TD00-600 is 2.534.

D. Aluminum Oxide

Aluminum oxide, Al_2O_3 in its stoichiometric form, is widely used in the visible and NIR due to its being reproducibly depositable, transparent, and quite highly thermally conductive. Aluminum oxide was sputtered using an aluminum target and O_2 flow rates of 1.8, 2.0, and 4.0 SCCM for samples

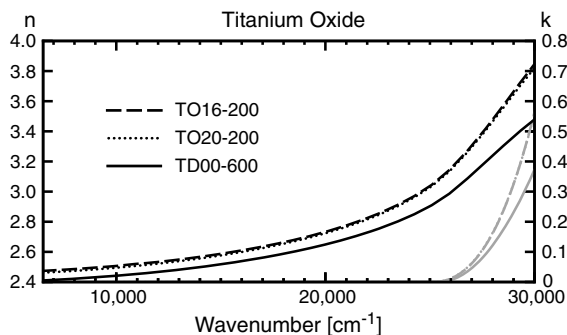


Fig. 9. Real (black curves) and imaginary (gray curves) parts of the refractive index for TiO_2 in the visible part of the spectrum for different reactive gas flow rates and targets. Note the different scales for n and k .

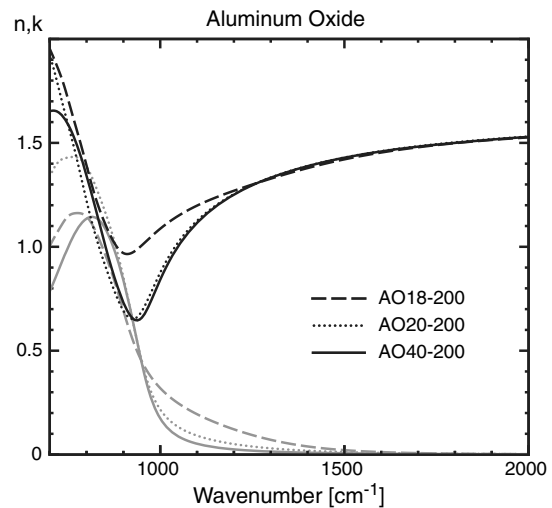


Fig. 10. Real (black curves) and imaginary (gray curves) parts of the refractive index for aluminum oxide in the further IR part of the MIR spectrum at different reactive gas flow rates.

AO18-200, AO20-200, and AO40-200, respectively. The samples have layer thicknesses of 368, 497, and 498 nm, respectively. Table 5 shows the Brendel oscillator parameters used to fit the spectra given in Figs. 10–12.

All samples are transparent starting at $\nu > 1590 \text{ cm}^{-1}$. Layers AO20-200 and AO40-200 are homogeneous, while layer AO18-200 has some incorporated contaminations over the first 30 nm (not shown). That structure was fitted with a two-layer system with a thin interface region. After the first 30 nm the layer deposited homogeneously; the optical properties are given for this region only. The process is very stable, yielding nearly identical optical properties for all flow rates, except for sample AO18-200, which deviates slightly around its main absorption (Fig. 10). The layers are optically thinner than literature values of stoichiometric bulk Al_2O_3 , e.g., at the He–Ne wavelength $n_{\text{AO40-200}} = 1.646$, whereas $n_{\text{lit}} \approx 1.76$ [13]. But the values agree well with values for thin films prepared by electron beam evaporation [19].

We conclude that all three samples are quite stoichiometric by way of the following argument: a higher Al concentration would raise the extinction

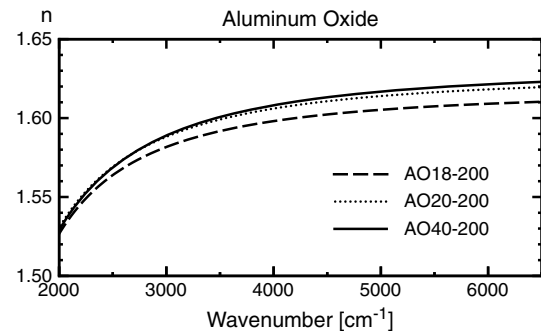


Fig. 11. Real refractive index for aluminum oxide in the nearer IR part of the MIR spectrum at different reactive gas flow rates.

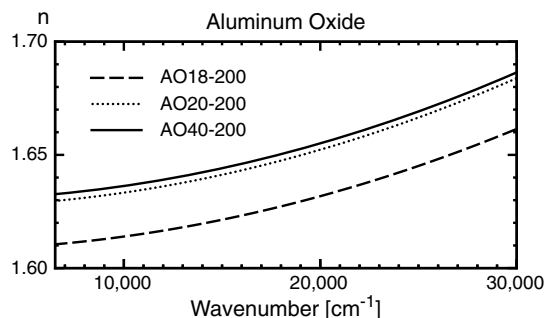


Fig. 12. Real refractive index for aluminum oxide in the visible part of the spectrum for different reactive gas flow rates.

coefficient substantially. Pure Al at 700 cm^{-1} has $k_{\text{Al}} \approx 112$ [20], whereas our samples have $k \approx 0.5\text{--}0.8$, even for sample AO18-200. Higher degrees of oxidation, i.e., aluminum (I) oxide and aluminum (II) oxide, require extreme conditions for formation, different from the one present during this sputter process [21,22]. The sputter rate was very small at approximately 1 nm/min at 200 W plasma power due to the hardness of the material. The absorption peak around 800 cm^{-1} in Fig. 10 does not have strong inhomogeneous broadening, indicating good small-distance ordering, similar to the case of SiO_2 .

E. Aluminum Nitride

Aluminum nitride sputtered using an Al target with different fluxes and powers shows that the layer properties have a great dependence on these parameters within the range tested here. Samples AN18-300 and AN20-300 were sputtered at 300 W plasma power using 1.8 and 2.0 SCCM nitrogen flow, respectively. Samples AN20-200 and AN40-200 were sputtered at 200 W using 2.0 and 4.0 SCCM , respectively. The ellipsometric measurements were fitted using the Brendel model. Table 6 shows the Brendel oscillator parameters used to fit the spectra given in Figs. 13–15. The samples AN18-300, AN20-300,

AN20-200, and AN40-200 had layer thicknesses of 220 , 297 , 207 , and 478 nm , respectively.

Sample AN18-300 is apparently strongly substoichiometric, with a significant unsaturated Al content contributing free carriers. This can be seen from the appreciable extinction coefficient over the entire wavenumber range in Figs. 13–15, with especially large values towards the low frequency limit in Fig. 13. Sample AN18-300 could not be well fitted with three oscillators like the other samples but required five for satisfactory results.

Samples AN20-300, AN20-200, and AN40-200 are transparent for $\nu > 1360\text{ cm}^{-1}$. All layers are homogeneous and amorphous, as can be inferred by the shape of the absorption peaks in Fig. 13.

Sample AN20-300, sputtered at a higher power, has a higher refractive index than samples AN20-200

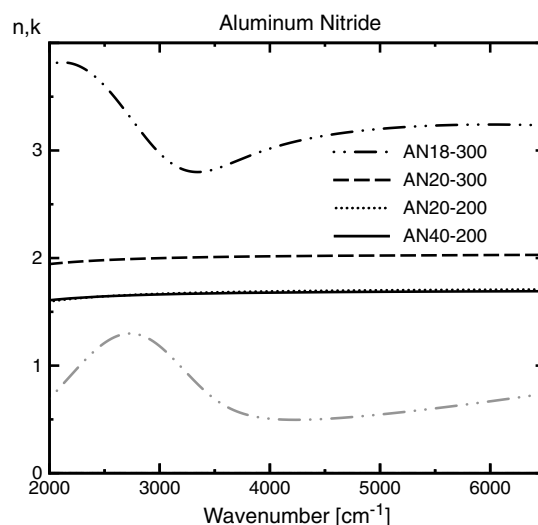


Fig. 14. Real (black curves) and imaginary (gray curves) parts of the refractive index for aluminum nitride in the nearer IR part of the MIR spectrum at different reactive gas flow rates.

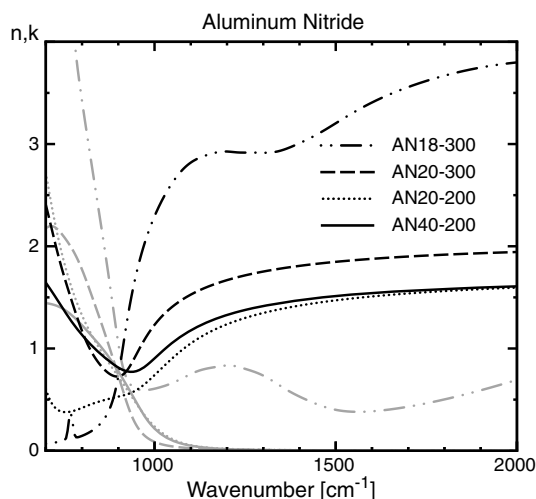


Fig. 13. Real (black curves) and imaginary (gray curves) parts of the refractive index for aluminum nitride in the further IR part of the MIR spectrum at different reactive gas flow rates.

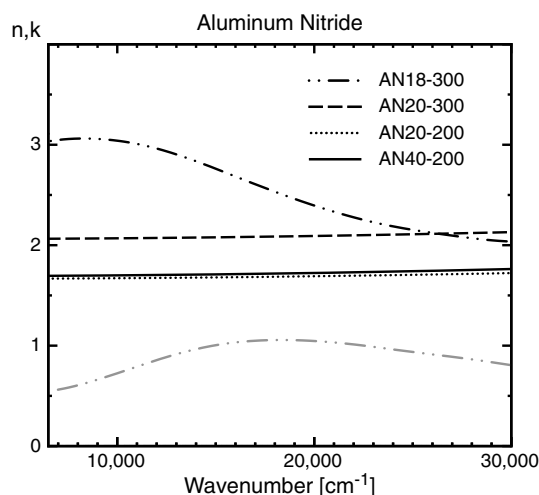


Fig. 15. Real (black curves) and imaginary (gray curves) parts of the refractive index for aluminum nitride in the visible part of the spectrum for different reactive gas flow rates.

and AN40-200. The literature values [23] for the index of refraction of sputtered AlN is between the values of samples AN20-300 and AN20-200, AN40-200. At the He–Ne wavenumber of $15,803\text{ cm}^{-1}$ the literature value is 1.92, for sample AN20-300 it is ≈ 2.10 , and for samples AN20-200 and AN40-200 it is ≈ 1.68 . Since it is known that AlN does not deposit overstoichiometrically [24], we conclude samples AN20-200 and AN40-200 are the saturated stoichiometric case, with reduced physical density. Thus Fig. 13 shows the optical response to a metal–dielectric transition.

The dependence on the plasma power comparing samples AN20-300 and AN20-200 is interesting. One sees that higher plasma power is consistent with lower nitrogen content. This is an illustration of the fact that plasma power determines the Al flux, while the N_2 flow determines the nitrogen availability independently; thus, to maintain stoichiometry at higher plasma power, a higher N_2 flow is also required. It is interesting to note that sample AN20-300 exhibits by far the highest sputter rate at 6.3 nm/min , as opposed to 2.8 , 1.4 , and 1.8 nm/min for samples AN18-300, AN20-200, and AN40-200, respectively.

5. Summary

We have deposited 38 samples (at 20 distinct process conditions) of the compound materials silicon oxide, silicon nitride, aluminum oxide, aluminum nitride, and titanium oxide, using reactive sputtering, each of which we have produced a series of samples for, with varying deposition conditions, and characterized them with respect to their MIR refractive index functions using variable angle spectroscopic ellipsometry. To facilitate comparison of the materials deposited in this work with others, the index of refraction was also measured in the NIR and VIS ranges of the spectrum.

As stoichiometric compounds we have found the following (each at 36 SCCM Ar flux): Si_3N_4 at 4 SCCM nitrogen flow and 300 W power with a Si target; SiO_2 at 4 SCCM oxygen flow and 200 W power with a Si target; AlN at 4 SCCM N_2 flow and 200 W power with an Al target; Al_2O_3 at 4 SCCM O_2 flow and 200 W power with an Al target; and TiO_2 nonreactively sputtered at 600 W power with a TiO_2 target.

Within the range of conditions that we investigated, SiO_2 , Al_2O_3 , and AlN were homogeneous, i.e., the sputter conditions were stable. In addition, SiO_2 and Al_2O_3 showed little variation when the conditions were varied within the probed limits. All materials showed little optical dispersion within their transparency regions.

We believe this information should be of great use for those seeking to produce low-tolerance optical coatings at arbitrary positions within the MIR part

of the optical spectrum without the use of expensive and potentially hazardous materials.

References

1. F. Tittel, D. Richter, and A. Fried, "Mid-infrared laser applications in spectroscopy," in *Solid-State Mid-Infrared Laser Sources* (Springer, 2003), pp. 458–529.
2. J. D. T. Kruschwitz and W. T. Pawlewicz, "Optical and durability properties of infrared transmitting thin films," *Appl. Opt.* **36**, 2157–2159 (1997).
3. K. Marsh and J. Savage, "Infrared optical materials for $8\text{--}13\text{ }\mu\text{m}$ —current developments and future prospects," *Infrared Phys.* **14**, 85–97 (1974).
4. P. Black and J. Wales, "Materials for use in the fabrication of infrared interference filters," *Infrared Phys.* **8**, 209–222 (1968).
5. P. Kelly and R. Arnell, "Magnetron sputtering: A review of recent developments and applications," *Vacuum* **56**, 159–172 (2000).
6. S. Berg, T. Larsson, C. Nender, and H.-O. Blom, "Predicting thin-film stoichiometry in reactive sputtering," *J. Appl. Phys.* **63**, 887–891 (1988).
7. H. Tompkins and E. Irene, *Handbook of Ellipsometry* (William Andrew, 2005).
8. G. Jellison and F. Modine, "Parameterization of the optical functions of amorphous materials in the interband region," *Appl. Phys. Lett.* **69**, 371–373 (1996).
9. J. Tauc, R. Grigorovici, and A. Vancu, "Optical properties and electronic structure of amorphous germanium," *Phys. Status Solidi B* **15**, 627–637 (1966).
10. H. Fujiwara, *Spectroscopic Ellipsometry: Principles and Applications* (Wiley, 2007).
11. J. Humlíček, "Sensitivity extrema in multiple-angle ellipsometry," *J. Opt. Soc. Am. A* **2**, 713–722 (1985).
12. R. P. Howson, "The reactive sputtering of oxides and nitrides," *Pure Appl. Chem.* **66**, 1311–1318 (1994).
13. E. Palik and G. Ghosh, *Handbook of Optical Constants of Solids* (Academic, 1998).
14. I. Malitson, "Interspecimen comparison of the refractive index of fused silica," *J. Opt. Soc. Am.* **55**, 1205–1208 (1965).
15. T. Bååk, "Silicon oxynitride; a material for grin optics," *Appl. Opt.* **21**, 1069–1072 (1982).
16. S. I. Lee, S. G. Rhee, and S. G. Oh, "Spectro-ellipsometric studies of sputtered amorphous titanium dioxide thin films: Simultaneous determination of refractive index, extinction coefficient, and void distribution," *J. Korean Phys. Soc.* **34**, 319–322 (1999).
17. S. Schiller, G. Beister, W. Sieber, G. Schirmer, and E. Hacker, "Influence of deposition parameters on the optical and structural properties of TiO_2 films produced by reactive d.c. plasmatron sputtering," *Thin Solid Films* **83**, 239–245 (1981).
18. M. Bass, ed., *Handbook of Optics* (McGraw-Hill, 2001).
19. K. S. Shamala, L. C. S. Murthy, and K. N. Rao, "Studies on optical and dielectric properties of Al_2O_3 thin films prepared by electron beam evaporation and spray pyrolysis method," *Mater. Sci. Eng. B* **106**, 269–274 (2004).
20. A. D. Rakić, "Algorithm for the determination of intrinsic optical constants of metal films: Application to aluminum," *Appl. Opt.* **34**, 4755–4767 (1995).
21. C. Dohmeier, D. Loos, and H. Schnoeckel, "Aluminum (I) and gallium (I) compounds: Syntheses, structures, and reactions," *Angew. Chem. Int. Ed.* **35**, 129–149 (1996).
22. D. Tyte, "Red ($B^2\Pi - A^2\Sigma$) band system of aluminium monoxide," *Nature* **202**, 383–384 (1964).
23. J. M. Khoshman and M. E. Kordes, "Optical characterization of sputtered amorphous aluminum nitride thin films by spectroscopic ellipsometry," *J. Non-Cryst. Solids* **351**, 3334–3340 (2005).
24. J. Harper, J. Cuomo, and H. Hentzell, "Synthesis of compound thin films by dual ion beam deposition. I. Experimental approach," *J. Appl. Phys.* **58**, 550–555 (1985).